PCCP

X-ray absorption spectroscopy insights on the structure anisotropy and charge transfer in Chevrel Phase chalcogenides

Journal:	*Physical Chemistry Chemical Physics*
Manuscript ID	CP-ART-10-2021-004851.R3
Article Type:	Paper
Date Submitted by the Author:	14-Jun-2022

Complete List of Authors:	Hyler, Forrest; University of California Davis Department of Chemistry, Chemistry Wuille Bille, Brian; University of California Davis Department of Chemistry, Chemistry Ortíz-Rodríguez, Jessica; University of California Davis Department of Chemistry, Chemistry Sanz Matías, Ana; Lawrence Berkeley National Laboratory, Molecular Foundry Roychoudhury, Subhayan; Lawrence Berkeley National Laboratory, Molecular Foundry Perryman, Joseph; University of California Davis Department of Chemistry, Chemistry Patridge, Christopher; D\'Youville College, Chemistry Singstock, Nicholas; University of Colorado Boulder, Chemical and Biological Engineering Musgrave, Charles; University of Colorado, Department of Chemical and Biological Engineering Velazquez, Jesus; University of California, Davis, Chemistry and Chemical Engineering

ARTICLE

X-ray absorption spectroscopy insights on the structure anisotropy and charge transfer in Chevrel Phase chalcogenides

Received 00th January 20xx,
Accepted 00th January 20xx

DOI: 10.1039/x0xx00000x

Forrest P. Hyler,*[a] Brian A. Wuille Bille,*[a] Jessica C. Ortíz-Rodríguez,[a] Ana Sanz Matías,[b] Subhayan Roychoudhury,[b] Joseph T. Perryman,[a] Christopher J. Patridge,[d] Nicholas R. Singstock,[e] Charles B. Musgrave,[e] David Prendergast ‡[b] and Jesús M. Velázquez ‡[a]

The electronic structure and local coordination of binary (Mo_6T_8) and ternary Chevrel Phases ($M_xMo_6T_8$) are investigated for a range of metal intercalant and chalcogen compositions. We evaluate differences in the Mo L_3-edge and K-edge X-ray absorption near edge structure across the suite of chalcogenides $M_xMo_6T_8$ (M = Cu, Ni, x = 1-2, T = S, Se, Te), quantifying the effect of compositional and structural modification on electronic structure. Furthermore, we highlight the expansion, contraction, and anisotropy of Mo_6 clusters within these Chevrel Phase frameworks through extended X-ray absorption fine structure analysis. Our results show that metal-to-cluster charge transfer upon intercalation is dominated by the chalcogen acceptors, evidenced by significant changes in their respective X-ray absorption spectra in comparison to relatively unaffected Mo cations. These results explain the effects of metal intercalation on the electronic and local structure of Chevrel Phases across various chalcogen compositions, and aid in rationalizing electron distribution within the structure.

Introduction

Since their first synthesis in 1971,[1] Chevrel Phases (CPs), $M_xMo_6T_8$ (M = metal; T = S, Se, Te), have demonstrated remarkable properties. Most notably, these properties lend themselves toward the use of CPs as high-temperature superconductors,[2,3] thermoelectrics,[4] multivalent cathode materials,[5–8] and catalysts.[9–11] Indeed, its unique pseudo-molecular structure endows CPs with a high degree of tunability of its electronic structure, including its valence and conduction band positions, band gaps, and orbital interactions with participating species in surface reactions. Hence, the electronic properties of these materials are sensitive to the identity and stoichiometry of the metal ion intercalant, M, as well as by the chalcogen identity, T.[12] However, while numerous studies have been performed by our group[10,11,13–15] and by the larger community exploring the electronic structure of sulphide binary and ternary CPs, comparatively less is known about their selenide and telluride analogs.[4,13,15–17]

The structure of CPs can be described as a network of cubic chalcogen cages that enclose a distorted octahedron of Mo atoms. As a result of their arrangement, the cage and octahedron that form each $M_xMo_6T_8$ cluster share a 3-fold rotational axis, rendering two chalcogen ions (T_2) of each cluster along this axis of symmetry as chemically distinguishable from the remaining six chalcogen ions due to their unique coordination environment (as seen in **Figure 1**).[18] In the extended CP structure, clusters are linked together by their chalcogen cages, which enable strong intercluster Mo-T and T-T interactions to yield a framework with voids that can host a range of metal cation stoichiometries.

In the binary CPs, the Mo_6 cluster is better described as a trigonal antiprism, which decreases in anisotropy as intercalant ions

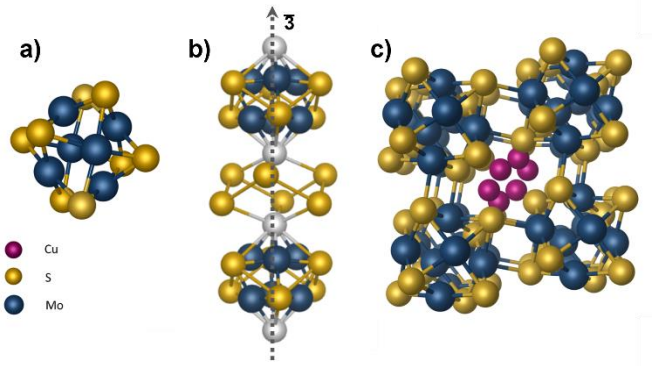

Figure 1. Crystal structure of the rhombohedral (R-3) CPs studied herein ($Cu_2Mo_6T_8$ T= S, Se) depicting a) an individual Mo_6T_8 cluster where the Mo atoms are represented in blue, and chalcogen atoms in gold, b) adjacent Mo_6T_8 clusters detailing a 3-fold rotational axis where cluster-linking undercoordinated chalcogens (T_2) are represented in white, and an intercluster cavity into which metals can be intercalated, and **c)** the $M_xMo_6T_8$ framework where intercalant metal atom sites are represented by magenta.

[a] Department of Chemistry, University of California, One Shields Avenue, Davis, California, 95616, USA.
[b] Molecular Foundry, Lawrence Berkeley National Laboratory, Berkeley, California, 94720, USA
[c] Department of Chemical Engineering, Stanford University, 443 Via Ortega, Stanford, California, 94305, USA
[d] Department of Chemistry, D'Youville College, 320 Porter Avenue, Buffalo, New York, 14201, USA.
[e] Department of Chemical and Biological Engineering, University of Colorado Boulder, Boulder, Colorado 80303, USA
* These authors contributed equally.
‡ Corresponding author. Email: dgprendergast@lbl.gov, jevelazquez@ucdavis.edu
Electronic Supplementary Information (ESI) available: Detailed experimental methods, including synthesis, characterization and XAS data analysis. See DOI: 10.1039/x0xx00000x

are inserted into the frameworks. This symmetry change has been previously explained as being the result of the electron density distribution within the Mo_6 octahedra (electronic factor)[19] as well as intercluster chalcogen repulsion that affects intracluster Mo-Mo bonding (geometric factor).[20] These electronic and geometric factor hypotheses agree with the observed contraction of the Mo_6 cluster upon intercalation of metal ions, which derives from the filling of Mo-Mo bonding states and the weakening of intercluster Mo-Mo and Mo-T bonds, respectively. A more detailed bond valence study that explored the nature of Mo_6-cluster anisotropy and its evolution upon cation insertion identified non-uniformity in anion charge distribution as the primary driver of intrinsic electronic instability of the binary sulphide phases, as well as the decrease in non-uniformity upon intercalation of small ions.[21] To provide additional insight regarding the aforementioned electronic structure and bonding formalisms for CPs, we present a detailed X-ray spectroscopic analysis of the interplay between electronic structure and local Mo-Mo and Mo-T coordination across an entire suite of binary and ternary CP chalcogenides.

X-ray Absorption Spectroscopy (XAS) is a uniquely well-suited technique for the study of these complex multinary systems, owing to its high elemental specificity and ability to provide valuable structural and electronic information. By means of X-ray absorption near-edge structure (XANES) analysis, exciton transitions are observed that can reveal critical information regarding the coordination environment of an absorbing species, as well as its oxidation and density of unoccupied electronic states.[22–24] Although intensity of the L_1 quadrupole transition edge (2s → 4d) is low, the more intense $L_{2,3}$ (2p → 4d) electric dipole transitions can instead be used to probe the oxidation state and electronic density around absorbing Mo ions in CPs without convolution from p-d mixing, and can thereby serve as a direct probe of covalency of transition metals regardless of their crystal field.[25] Furthermore, lattice geometry can be determined through extended X-ray absorption fine structure (EXAFS) analysis that reveals structural distortions and bond distance information. This is accomplished through excitation by photons of energy greater than the absorption edge, which produces photoemitted electrons. Interference between outgoing wave components of the photoemitted electron from the X-ray excited atom and backscattered components from neighbouring atoms provides information related to the interatomic distances between the absorber atom and those in its surrounding coordination shells. The combination of analyses in both regions of the XAS spectrum helps explain the charge transfer phenomena and differences in the structural properties of intercalated and binary Mo_6T_8 frameworks.

Herein, we report the analyses of XANES and EXAFS experiments that corroborate arguments regarding how metal intercalation into the CP sulphide, selenide, and telluride frameworks control cluster anisotropy, cavity deformation, and charge transfer. This work highlights the intricate effects of ternary intercalation on structure and electronic properties for a highly versatile material family, and thereby provides valuable insights that may inform and accelerate the design of new compositions with a variety of applications.

Results and discussion

Synthesis and Structural Characterization

Pure-phase binary and metal-intercalated CPs with the Mo_6S_8, Mo_6Se_8, Mo_6Te_8, $Cu_2Mo_6S_8$, $Cu_2Mo_6Se_8$, and $NiMo_6Te_8$ compositions were obtained through a rapid microwave-assisted solid-state synthesis approach described in our previous work,[10,11,13–15] with this being the first expansion of the synthesis approach to produce metal-intercalated CP selenides. Scanning electron microscopy (SEM) images reveal the faceted, polycrystalline morphology of these phases (**Figure 2a-c**; **Figure S1a-c**). A slight decrease in crystallinity was observed for the telluride phase, which agrees with the broader and less intense diffraction peaks for $NiMo_6Te_8$ compared to Cu_2MoS_8 and $Cu_2Mo_6Se_8$. The powder X-ray diffraction (PXRD) patterns for each CP are in close agreement with literature and indicate a rhombohedral crystal phase for $Cu_2Mo_6Se_8$, $Cu_2Mo_6S_8$, Mo_6S_8, Mo_6Se_8 and Mo_6Te_8 (**Figure 2d,e**; **Figure S1 d-f**). Additional diffraction peaks associated with a triclinic distortion are observed for $NiMo_6Te_8$, which agrees with results reported for the similar $Ni_{0.85}Mo_6Te_8$ composition (**Figure 2f**).[26] All the phases synthesized in this work share a diffraction peak at $2\theta \cong 12°$, which is characteristic of CPs and corresponds to diffraction from the (101) and (010) planes for the rhombohedral and triclinic phases, respectively. A noticeable shift of this peak to lower 2θ values (Te<Se<S) was observed as the ionic radius of the chalcogen increases (S<Se<Te), agreeing with the increase in the unit cell volume (**Figure S2**). Additionally, a slight shift in 2θ to lower values for the rhombohedral structures was observed upon metal intercalation—a feature that is noticeably more pronounced for CP selenides (Mo_6Se_8<<$Cu_2Mo_6Se_8$) than sulphides (Mo_6S_8<$Cu_2Mo_6S_8$) (**Figure S2**). This appears to be the result of reduced chalcogen-intercalant attraction in $Cu_2Mo_6Se_8$ relative to $Cu_2Mo_6S_8$, which arises due to the decreased chalcogen electronegativity and resultant lack of electrostatic attraction between the Mo_6Se_8 cluster and the interstitial cation species linking them together.[15]

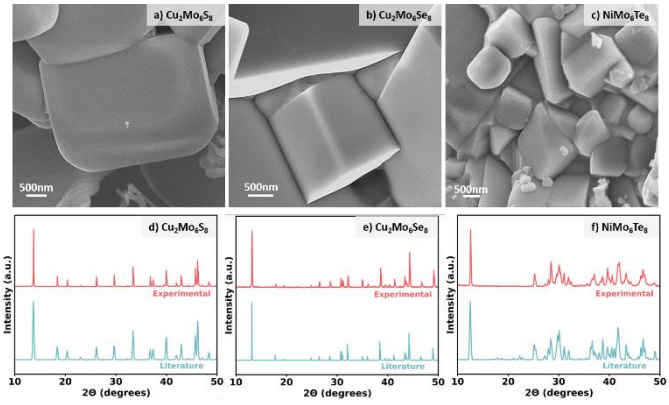

Figure 2. a) SEM micrographs of a) $Cu_2Mo_6S_8$, b) $Cu_2Mo_6Se_8$ and c) $NiMo_6Te_8$ along with their corresponding PXRD diffractograms d) - f).

Local Structure Distortion Upon Intercalation

As previously mentioned, metal intercalation has a marked effect on the electronic and geometric structures of CPs. More specifically, insertion of metal ions into the cavities between Mo_6T_8 clusters induces alterations not only to the intercluster Mo-Mo, Mo-T, and T-T distances, but also to the intracluster Mo-Mo distances of the Mo_6 trigonal antiprism. Thus, to understand the extent to which the host structure is modified by the ternary intercalant species, Mo K-edge EXAFS analysis was performed for Mo_6S_8, $Cu_2Mo_6S_8$, Mo_6Se_8, $Cu_2Mo_6Se_8$, Mo_6Te_8, and $NiMo_6Te_8$ CPs. Fourier-transformed EXAFS data, including magnitudes and real components, and corresponding fitted plots for the binary and intercalated sulphides, selenides, and tellurides are showcased for comparison in **Figure 3**.

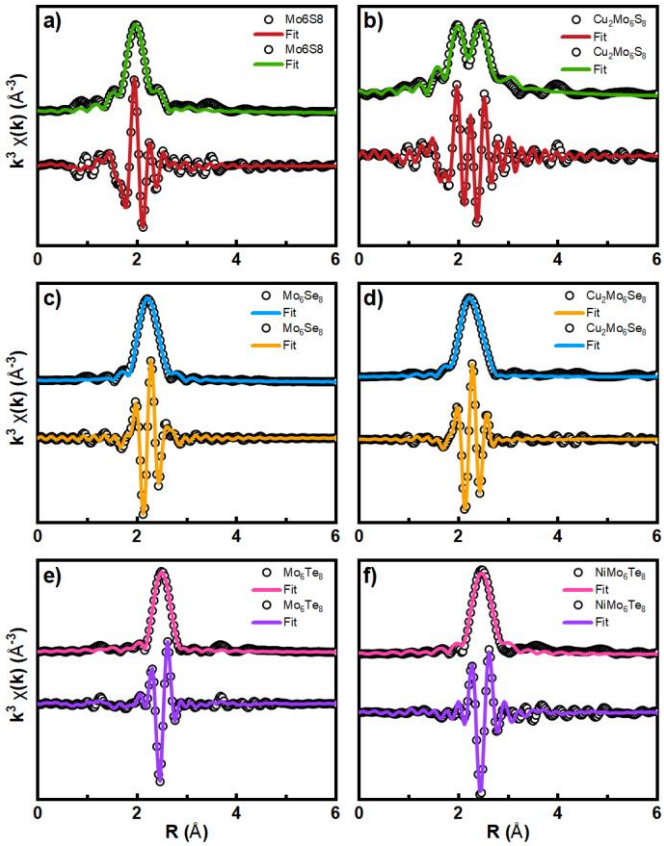

Figure 3. Mo K-edge FT-EXAFS data (circles) and fits (solid lines) showing the non-phase-corrected magnitude (top lines) and real (bottom lines) components of the Fourier transform of $k^3\chi(k)$ in radial space for the sulphide, selenide, and telluride binary CPs (a, c, and e), and the Cu intercalated sulphide and selenide (b, d), and Ni intercalated telluride CPs (f).

Upon X-ray irradiation above the Mo K-edge energy (20 keV), generated photoelectrons scatter from the neighbouring atoms surrounding the absorbing element. Due to the overlapping edges of the sulphur K-edge and molybdenum L_3-edge, the Mo K-edge was chosen for EXAFS fitting due to the non-interferent nature of the photoelectrons produced at the energy utilized, as well as the wealth of structural information extractable for the intercluster and intracluster Mo-Mo and Mo-T bonding landscape. Contributing scattering paths to the EXAFS signal are represented in **Figure 4** and extracted distances from fitted data are detailed in **Table S1**. $Cu_2Mo_6Se_8$ and especially $Cu_2Mo_6S_8$ demonstrate appreciable increases in their intercluster Mo-T distances relative to their binary analogues of 0.1 and 0.03 Å, respectively. This increase in path length is consistent with the incorporation of multiple ions per cavity.

The introduction of intercalant metal ions causes structural transformations in both the chalcogen cage and the Mo_6 cluster. To quantify this structural shift, we monitored cluster anisotropy. The cluster anisotropy is defined here as the quotient between the longest and shortest Mo-Mo bond distances in the trigonal antiprism (**Table 1**). In conjunction with the elongation of intercluster Mo-T bonds, our results indicate a reduction in cluster anisotropy between the binary CPs and their respective ternary analogues, in good agreement with previous reports (**Table 1**).[21] In binary CPs, the two chalcogen ions located along the 3-fold rotation axis have a lower coordination number than the remaining 6 of the Mo_6T_8 cluster (**Figure 1b)**. Thus, the lack of dative interactions from the chalcogen to neighbouring clusters induces the undercoordinated chalcogens to bare a more negative charge, as demonstrated by Hughbanks and Hoffmann.[27] Upon intercalation, the occupation of intercluster cavities mitigates the undercoordination of these chalcogen sites and distributes their valency more evenly amongst the other chalcogen atoms.

In the case of the intercalated telluride phase ($NiMo_6Te_8$), the cluster anisotropy shows a remarkable increase in comparison to the binary. This could be rooted in the lower electronegativity of the Te ions, thus leading to a lower degree of charge transfer with the intercalant cations, as well as in the distinct space groups between the binary and ternary telluride CPs. The triclinic crystal structure of $NiMo_6Te_8$, which lacks the 3-fold rotation axis of symmetry present in Mo_6Te_8, may impose a lower symmetry on the entire chalcogen cage, thus resulting in an inherently asymmetric Mo_6 cluster. To attain a clear understanding of the structural symmetry of the intercalated CP tellurides, more EXAFS studies over a large composition spectrum are required.

Chevrel Phase	Cluster e-count	Cluster Anisotropy (%)
Mo_6S_8	20	8.85 ± 1.63
$Cu_2Mo_6S_8$	22	4.44 ± 1.64
Mo_6Se_8	20	5.55 ± 2.15
$Cu_2Mo_6Se_8$	22	3.70 ± 1.52
Mo_6Te_8	20	4.73 ± 0.50
$NiMo_6Te_8$	22	11.04 ± 0.43

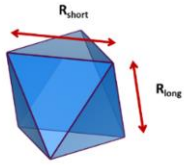

Table 1. Cluster anisotropy relationship to the cluster valence electron count (VEC). The anisotropy was calculated following ref. 21, as $(R_{long}-R_{short})x100/R_{long}$, where R depicts the interatomic distance between intracluster Mo atoms as obtained from Mo K edge EXAFS data (distances can be visualized in the blue polyhedron with each vertex representing a Mo atom). VEC was calculated according to ref. 21.

Charge Transfer in Chevrel Phases

Mo L_3-, S K-, Se K-, and Te L_3-edge excitations were probed to evaluate metal–chalcogen interactions and electron density distribution in each CP. It is known that Mo 4d orbitals play a critical role in previously observed S pre-edge features due to hybridization between Mo 4d and S 3p orbitals.[6,19] Vacant hybrid orbitals enhance the pre-edge region observed in the S K-edge. The addition of electron density to these hybridized orbitals from a ternary intercalant acting as an electron donor results in a depressed pre-edge peak, as observed in **Figure 5b**. Additionally, interactions between Mo and T have a substantial effect on the Mo L_3-edge absorption edge position and can provide additional electronic information for the Se and Te congeners, allowing for further analysis of the role that chalcogen electronegativity has on electron distribution within the cluster.

Inspection of the Mo L_3-edge position shown in **Figure S4** reveals the effect of ion intercalation on the valency of the Mo_6 host. Both sulphide and selenide CPs exhibit a red-shifted Mo L_3-

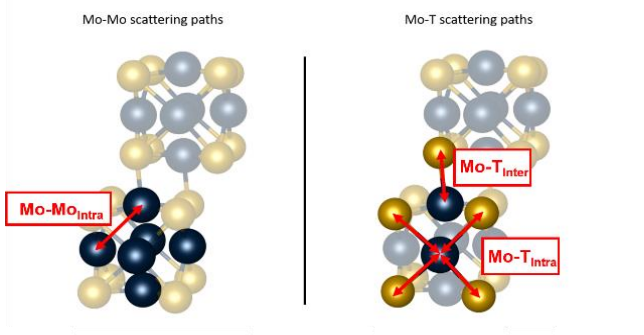

Figure 4. Graphic representation of the intracluster and intercluster scattering paths observed in **Figure 3** for 1s photoelectrons between an absorbing Mo and its neighbouring Mo and T ions in the CP framework. Information for each path is detailed in **Table S1**.

edge after 2 equivalents of Cu have been intercalated into the cavities. This lower absorption energy indicates a more reduced Mo species following electron donation from the intercalant into the cluster, subsequent redistribution of chalcogen valency, and resultant contraction of the clusters (**Figure 3**). Conversely, the telluride CP displays an opposite trend, with a small blue shift in the Mo L_3-edge following Ni intercalation. This observation is in good agreement with the previously described expansion of the Mo_6Te_8 cluster after intercalation (vide supra and detailed in **Table S1**). Bond lengthening upon metal intercalation of Mo_6Te_8 clusters develops a lower overall electron density of the molybdenum atoms. While perceptible, these energy shifts are small in magnitude, which is consistent with the general low redox activity of the Mo centres upon intercalation.[17,28] It is noteworthy that the effect of chalcogen composition and—more importantly—chalcogen electronegativity manifests itself in the electronic structure of the Mo_6 trigonal antiprism, as seen in the progressively blue-shifted Mo L_3-edge centroids in **Figure 5a** along the series Mo_6Te_8<Mo_6Se_8<Mo_6S_8. Specifically, and perhaps intuitively, a more oxidized molybdenum species predominates as the chalcogen electronegativity increases. This result is of high importance, as Mo atoms are known to be the adsorption site of small molecules in catalytic applications,[9,13] hence selectively engendering programmable valency to these sites may afford a fine level of control over reactivity for a suite of applications. As a result of this promise for tuning Mo reactivity based upon chalcogen electronegativity, additional in-situ and in-operando Mo XANES measurements are warranted that may elucidate the nature of Mo-adsorbate interactions during relevant reactions such as the CO_2 reduction and C-C coupling reactions.

Much like the Mo edges, chalcogen absorption edges provide valuable insight into the charge transfer phenomenon that occurs during ternary intercalation into CPs. Among these edges, the S K-edge illustrates the pronounced effect of intercalant-to-chalcogen charge transfer. As can be seen in **Figure 5b**, a modest red shift of the white line position is detected upon intercalation, although a rather abrupt decrease in the pre-edge (located around 2470.5 eV) intensity is observed, indicating significant population of previously unoccupied hybridized S 3p/Mo 4d states that are responsible for the pre-edge feature intensity. This population of 3p states by Cu-donated electron density effectively depresses the pre-edge feature in the intercalated $Cu_2Mo_6S_8$ structure relative to the binary Mo_6S_8 that retains its unoccupied S 3p states that can accept excited electrons during the S 1s → S 3p/Mo 4d transition. This effect is more clearly visible from the analysis of the second derivatives of the corresponding spectra shown in **Figure S6a** where the binary sulphide CP exhibits two well-resolved peaks centred around 2470 eV. These peaks merge into a single signal upon intercalation of two copper equivalents and subsequent introduction of the intercalant electron density. Small metal cations such as Cu^+ are known to occupy the cavity in a perpendicular fashion to the 3-fold rotation axis of the CP framework highlighted in **Figure 1b-c**,[17] in closest proximity to undercoordinated S sites. Upon intercalation, electron density from the ternary cation is transferred to empty (4d hybridized) S 3p orbitals that are responsible for the pre-edge feature. As a result of orbital occupation from intercalant-induced electron transfer, the spectra show a reduced intensity in the absorption pre-edge signal in the S K-edge XANES. The two resolved peaks at 2470 eV for the S-K 2nd derivative are merged to a single broad feature and this can be interpreted as a more uniform S valency distribution and coordination environment and, consequently, a less anisotropic Mo_6 trigonal antiprism.[18,19]

The S K-edge spectra of Mo_6S_8 an $Cu_2Mo_6S_8$ (**Figure 5b**, dashed lines) were calculated using the many-body X-ray absorption spectroscopy method (MBXAS),[29–31] a density functional theory-based methodology that computes the absorption cross-section by approximating each electronic state (i.e., the initial state and each of the final states) as a Slater determinant (see Computational Details in the SI). The anisotropy of the simulated structural models is, respectively, 5.76 % and 3.31%, in excellent agreement with experiment (**Table 1**), as are the spectra. Bader charge analysis of the Mo_6S_8 and $Cu_2Mo_6S_8$ structures confirms that the intercalant-induced electron transfer is mostly to the previously undercoordinated S_2 sites (see **Table S9**), which are reduced by 0.16 e^-. On the other hand, the Mo and the tetracoordinated S_1 sites are reduced by less than 0.08 e^-. The charge on S_1 and S_2 sites equalizes to ~ –0.80 e^- in the intercalated phase, reflecting the reduced cluster anisotropy of $Cu_2Mo_6S_8$ and their corresponding atomic contributions to the overall spectrum bear closer resemblance to one another (**Figure S8**), leading to the disappearance of the pre-edge. The strong-blue shift in the S_2 spectra is mainly due to the presence of the Cu, rather than the geometric changes associated with it. Counterintuitively, the steepness of the pDOS near the Fermi level indicates a decrease in charge carriers when Cu is added and the Fermi level raised. This results in decreased screening, hence the blue-shift (See SI Section *Effect of geometric changes and charge transfer on spectra*). We note that, in contrast to the expected greater negativity of the undercoordinated S_2 atom, Bader charges indicate less negative charge on these sites. However, the associated atomic volume for these atoms is quite large, due to the open structure of the lattice, and a more localized charge estimate (Löwdin charge) does indeed indicate that S_2 is slightly more reduced than S_1 (**Table S8**).

In the case of the Se K-edge, there is no appreciable pre-edge feature and no change in intensity of the edge is noticeable upon intercalation. This may be rooted in a lower degree of Mo d – T p orbital hybridization as a result of a larger orbital energy mismatch between the elements. In addition, the lack of well-defined pre-edge absorption peaks in the heavier chalcogens is consistent with the decrease in the core-hole lifetime of their corresponding high energy edges compared to sulphur.

Cu-intercalated selenide and Ni-intercalated telluride CPs both demonstrate a decrease in absorption onset energies in their respective chalcogen XANES spectra, in good agreement with more reduced Se and Te species. In comparing the Mo L_3-edge spectra for the CPs studied here (**Figure S4**), the electronic structure changes as evidenced by shifting chalcogen absorption edges indicate that charge transfer occurs primarily from the intercalant to the chalcogen cages, rather than directly to the Mo_6 core, despite the redistribution of Mo valency upon intercalation. However, this M-to-T electron transfer shows good agreement with previous results published by Prendergast et al.[32] These changes in absorption edge positions and intensities highlight the significance of identifying useful sites within the CP structure that are amenable to selectively accepting electron density during intercalation by a ternary species.

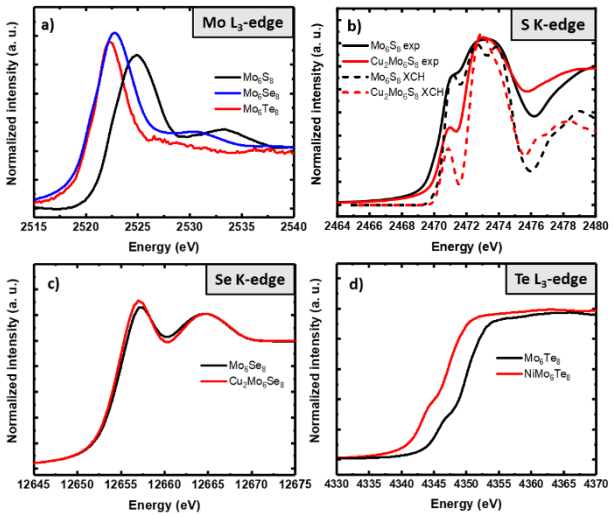

Figure 5. Molybdenum and chalcogen XANES spectra for binary and ternary Chevrel phases. (a) Mo L_3-edge of sulphide, selenide and telluride CPs, (b) S K-edge of Mo_6S_8 and $Cu_2Mo_6S_8$, the calculated spectra are shown with dashed lines (c) Se K-edge of Mo_6Se_8 and $Cu_2Mo_6Se_8$, and (d) Te L_3-edge of Mo_6Te_8 and $NiMo_6Te_8$.

Conclusions

We have presented an extensive XAS study on the atomistic and electronic structure of Chevrel Phases and on their evolution upon intercalation by a ternary species. Results extracted from Mo K-edge EXAFS confirm the reduction of Mo_6 cluster anisotropy after metal insertion, which we attribute to a more evenly distributed chalcogen valency. Modulated charge density of the Mo_6 cluster as a function of chalcogen electronegativity was also evidenced by a red shift in the Mo L_3-edge absorption edge centroid for the binary series Mo_6T_8 with a decrease in energy as the electronegativity of the chalcogen decreases. Additionally, by comparing the Mo L_3- and chalcogen K- and L_3- edge XANES of binary and metal-intercalated CPs, it was concluded that charge transfer is mediated by the chalcogen, with the most noticeable effects observed for the S K pre-edge feature and Te L_3-edge red-shift after metal intercalation. The results of this work provide a detailed view of the effect of intercalation on the atomic structure and anisotropy of Chevrel Phase sulphide, selenide and tellurides. Furthermore, the effect of the chalcogen identity on the Mo cluster electronic structure and its change after interaction with the ternary cation in $M_xMo_6T_8$ phases suggest how the ternary CPs may be rationally tuned for their applications of interest.

Author Contributions

The manuscript was written through contributions of all authors. All authors have given approval to the final version of the manuscript.
*These authors contributed equally.

Author Information

Forrest P. Hyler – Department of Chemistry, University of California, Davis, One Shields Avenue, Davis, California 95616, United States; https://orcid.org/0000-0002-7397-8013

Brian A. Wuille Bille – Department of Chemistry, University of California, Davis, One Shields Avenue, Davis, California 95616, United States; https://orcid.org/0000-0003-2745-2499

Jessica C. Ortíz-Rodríguez – Department of Chemistry, University of California, Davis, One Shields Avenue, Davis, California 95616, United States; https://orcid.org/0000-0002-1506-5654

Ana Sanz Matías – Molecular Foundry, Lawrence Berkeley National Laboratory, Berkeley, California 94720, United States

Subhayan Roychoudhury – Molecular Foundry, Lawrence Berkeley National Laboratory, Berkeley, California 94720, United States

Joseph T. Perryman – Department of Chemical Engineering, Stanford University, 443 Via Ortega, Stanford, California 94305, United States; https://orcid.org/0000-0002-3170-8007

Christopher J. Patridge – Department of Chemistry, D'Youville College, 320 Porter Avenue, Buffalo, NY 14201, United States; https://orcid.org/0000-0002-0454-2873

Nicholas R. Singstock – Department of Chemical and Biological Engineering, University of Colorado Boulder, Boulder, Colorado 80303, United States; https://orcid.org/0000-0003-2093-0216

Charles B. Musgrave – Department of Chemical and Biological Engineering, Materials Science and Engineering Program, and Renewable and Sustainable Energy Institute, University of Colorado Boulder, Boulder, Colorado 80303, United States; https://orcid.org/0000-0002-5732-3180

David Prendergast – Molecular Foundry, Lawrence Berkeley National Laboratory, Berkeley, California 94720, United States; https://orcid.org/0000-0003-0598-1453

Jesús M. Velázquez – Department of Chemistry, University of California, Davis, One Shields Avenue, Davis, California 95616, United States; https://orcid.org/0000-0003-2790-0976

Conflicts of interest

The authors declare no conflicts of interest.

Acknowledgements

JMV thanks the University of California, Davis for start-up funding. JMV also acknowledges support from the Cottrell Scholars program supported by the Research Corporation for Science Advancement (RCSA 26780), as well as support from the National Science Foundation through the Faculty Early Career Development Program (DMR-2044403). JOR was funded by the National Science Foundation Graduate Research Fellowship (NSF 1650042). Part of this study was carried out at the UC Davis Center for Nano and Micro Manufacturing (CNM2). Use of the Stanford Synchrotron Radiation Lightsource, SLAC National Accelerator Laboratory, is supported by the U.S. Department of Energy, Office of Science, Office of Basic Energy Sciences under Contract No. DE-AC02-76SF00515. This research used resources of the National

Synchrotron Light Source, a U.S. Department of Energy (DOE) Office of Science User Facility operated for the DOE Office of Science by Brookhaven National Laboratory under Contract No. DE-AC02-98CH10886. DFT calculations and X-ray spectral analysis were performed by ASM, SR, and DP using resources of the National Energy Research Scientific Computing Center (NERSC), a U.S. Department of Energy Office of Science User Facility located at Lawrence Berkeley National Laboratory, operated under Contract No. DE-AC02-05CH11231. Spectral analysis was facilitated through a user project at the Molecular Foundry at Lawrence Berkeley National Laboratory, which is supported by the Office of Science, Office of Basic Energy Sciences, of the U.S. Department of Energy under Contract No. DE-AC02-05CH11231. NRS and CBM acknowledge support by the National Science Foundation (CBET-2016225).

References

1 R. Chevrel, M. Sergent and J. Prigent, *J. Solid State Chem.*, 1971, **3**, 515–519.
2 G. V. Subba Rao and G. Balakrishnan, *Bull. Mater. Sci.*, 1984, **6**, 283–316.
3 Ø. Fischer, *Appl. Phys.*, 1978, **16**, 1–28.
4 X. ya Shi, L. Wang, L. D. Chen and X. H. Chen, *Trans. Nonferrous Met. Soc. China (English Ed.*, 2009, **19**, 642–645.
5 A. Mitelman, M. D. Levi, E. Lancry, E. Levi and D. Aurbach, *Chem. Commun.*, 2007, 4212–4214.
6 D. Muthuraj and S. Mitra, *Mater. Res. Bull.*, 2018, **101**, 167–174.
7 E. Lancry, E. Levi, Y. Gofer, M. Levi, G. Salitra and D. Aurbach, *Chem. Mater.*, 2004, **16**, 2832–2838.
8 P. Yu, X. Long, N. Zhang, X. Feng, J. Fu, S. Zheng, G. Ren, Z. Liu, C. Wang and X. Liu, *J. Phys. Chem. Lett.*, 2019, **10**, 1159–1166.
9 K. M. Kadiev, S. N. Khadzhiev, M. K. Kadieva and E. S. Dogova, *Pet. Chem.*, 2017, **57**, 608–617.
10 J. T. Perryman, F. P. Hyler, J. C. Ortiz-Rodríguez, A. Mehta, A. R. Kulkarni and J. M. Velázquez, *J. Coord. Chem.*, 2019, **72**, 1322–1335.
11 J. T. Perryman, J. C. Ortiz-Rodríguez, J. W. Jude, F. P. Hyler, R. C. Davis, A. Mehta, A. R. Kulkarni, C. J. Patridge and J. M. Velázquez, *Mater. Horizons*, 2020, **7**, 193–202.
12 O. K. Andersen, W. Klose and H. Nohl, *Phys. Rev. B*, 1978, **17**, 1209–1237.
13 J. C. Ortiz-Rodríguez, N. R. Singstock, J. T. Perryman, F. P. Hyler, S. J. Jones, A. M. Holder, C. B. Musgrave and J. M. Velázquez, *ACS Appl. Mater. Interfaces*, 2020, **12**, 35995–36003.
14 K. Lilova, J. T. Perryman, N. R. Singstock, M. Abramchuk, T. Subramani, A. Lam, R. Yoo, J. C. Ortiz-Rodríguez, C. B. Musgrave, A. Navrotsky and J. M. Velázquez, *Chem. Mater.*, 2020, **32**, 7044–7051.
15 N. R. Singstock, J. C. Ortiz-Rodríguez, J. T. Perryman, C. Sutton, J. M. Velázquez and C. B. Musgrave, *J. Am. Chem. Soc.*, 2021, **143**, 9113–9122.
16 F. J. Berry, E. M. Forgan and C. D. Gibbs, *Solid State Commun.*, 1988, **66**, 667–670.
17 F. J. Berry and C. D. Gibbs, *Solid State Commun.*, 1992, **83**, 517–520.
18 J. K. Burdett and J. H. Lin, *Inorg. Chem.*, 1982, **21**, 5–10.
19 F. Kubel and K. Yvon, *J. Solid State Chem.*, 1988, **73**, 188–191.
20 J. D. Corbett, *J. Solid State Chem.*, 1981, **39**, 56–74.
21 E. Levi and D. Aurbach, *Chem. Mater.*, 2010, **22**, 3678–3692.
22 T. K. Sham, *Phys. Rev. B*, 1985, **31**, 1888–1902.
23 F. Farges and G. E. Brown, *Phys. Rev. B - Condens. Matter Mater. Phys.*, 1997, **56**, 1809–1819.
24 M. Tromp, J. Moulin, G. Reid and J. Evans, *AIP Conf. Proc.*, 2007, **882**, 699–701.
25 M. L. Baker, M. W. Mara, J. J. Yan, K. O. Hodgson, B. Hedman and E. I. Solomon, *Coord. Chem. Rev.*, 2017, **345**, 182–208.
26 K. Hönle, W.; Yvon, *J. Solid State Chem.*, 1987, **240**, 235–240.
27 T. Hughbanks and R. Hoffmann, *J. Am. Chem. Soc.*, 1983, **105**, 1150–1162.
28 K. Asokan, O. Peña, L. Le Polles, J. C. Jan, J. W. Chiou and W. F. Pong, *J. Clust. Sci.*, 2009, **20**, 205–211.
29 Y. Liang, J. Vinson, S. Pemmaraju, W. S. Drisdell, E. L. Shirley and D. Prendergast, *Phys. Rev. Lett.*, 2017, **118**, 1–7.
30 Y. Liang and D. Prendergast, *Phys. Rev. B*, 2019, **100**, 1–12.
31 Y. Liang and D. Prendergast, *Phys. Rev. B*, 2018, **97**, 1–25.
32 L. F. Wan, J. Wright, B. R. Perdue, T. T. Fister, S. Kim, C. A. Apblett and D. Prendergast, *Phys. Chem. Chem. Phys.*, 2016, **18**, 17326–17329.